CrystEngComm

ROYAL SOCIETY OF CHEMISTRY

PAPER

View Article Online
View Journal | View Issue

Cite this: *CrystEngComm*, 2021, **23**, 3549

The exceptionally high moisture responsiveness of a new conductive-coordination-polymer based chemiresistive sensor†

Yuan Lin,[ab] Huijie Jiang,[c] Guangling Liang,[a] Wei-Hua Deng,[ab] Qiaohong Li, *[a] Wen-Hua Li *[a] and Gang Xu [a]

A new conductive coordination polymer (CCP), Ag(SPh–NO_2)·$AgNO_3$, with a three-dimensional (3D) non-porous structure composed of a unique 2D inorganic layered structure linked by an organic linker, was reported. The 3D CCP Ag(SPh–NO_2)·$AgNO_3$ exhibits semiconductor behavior, with electronic conductivity as high as 2.7×10^{-6} S cm^{-1} at 295 K, which is comparable to the vast majority of highly conductive 3D coordination polymers. The chemiresistive humidity sensing ability of Ag(SPh–NO_2)·$AgNO_3$ was studied over a wide relative humidity (RH) range (10–90% RH) at room temperature. The sensor showed exceptionally high moisture responsiveness, with a 10^6-fold increase in response at 90% RH and excellent sensitivity to humidity in the range of 10–80% RH. The sensing mechanism was further studied using alternating current (AC) impedance spectroscopy and direct current (DC) instantaneous reverse polarity experiments. The exceptionally high response of the Ag(SPh–NO_2)·$AgNO_3$-based sensor at high RH is attributed to the periodic arrangement of the ion species *via* reversible coordination bonds in the structure. H_3O^+ and Ag^+ are easily formed on its hydrophilic surface, through which the free transport of ionic carriers dominates the conductivity change. Using density functional theory (DFT) calculations, it is further demonstrated that the reversibly coordinated $AgNO_3$ in the structure can be easily occupied by water molecules, which is thermodynamically spontaneous in the presence of humidity. Furthermore, the functional $AgNO_3$ groups and their reversible coordination bonds enabled Ag(SPh–NO_2)·$AgNO_3$ to show exceptionally high moisture responsiveness.

Received 12th March 2021,
Accepted 14th April 2021

DOI: 10.1039/d1ce00347j

rsc.li/crystengcomm

Introduction

As an integral part of the internet of things, gas sensors have attracted great attention due to their widespread applications in environmental supervision, food quality control and physiological detection.[1–3] Among the many types of gas sensors, chemiresistive gas/humidity sensors are increasingly gaining prominence for their simplicity, low cost and power consumption, and ease of integration with standard electronics.[4–10] Over the past few decades, various chemiresistive sensing materials, such as metal oxide semiconductors,[11–14] organic polymers,[15] graphene and its composites,[16,17] transition metal dichalcogenides[18,19] and MXene,[20] have been studied. However, their higher operating temperature, non-crystalline structures or partially and disorderedly arranged functional groups present challenges in terms of achieving low power consumption, high sensitivity and insight into the structure–sensing relationships. Humidity is an inevitable constituent of our environment and can vary with season and temperature. Humidity sensing is indispensable in every aspect of life, such as agricultural and industrial production, food storage and human life.[21] At present, novel materials with exceptionally high humidity responsiveness, insightful sensing mechanism exploration and good stability are still desired.

In contrast to traditional chemiresistive sensing materials, novel functional material design utilizing coordination chemistry is a powerful approach because of the structural designability of such materials and ease of structural characterization through single crystal X-ray diffraction (SXRD) techniques. Coordination polymers (CPs), which are a representative type of coordination complexes and are constructed by metal centers and organic ligands *via* self-

[a] *State Key Laboratory of Structural Chemistry, Fujian Institute of Research on the Structure of Matter, Chinese Academy of Sciences (CAS), 155 Yangqiao Road West, Fuzhou, Fujian 350002, P. R. China. E-mail: lqh2382@fjirsm.ac.cn, whli@fjirsm.ac.cn*

[b] *University of Chinese Academy of Sciences, Chinese Academy of Sciences, Beijing 100049, China*

[c] *Institute of Materials in Electrical Engineering 1 (IWE1), RWTH Aachen University, Sommerfeldstrasse 24, 52074 Aachen, Germany*

† Electronic supplementary information (ESI) available. CCDC 2052741. For ESI and crystallographic data in CIF or other electronic format see DOI: 10.1039/d1ce00347j

assembly interactions, have aroused great interest due to their defined structure, robust chemical tunability and multifunctionality.[22,23] Recently, several examples of chemiresistive sensors based on CPs have been developed for room-temperature humidity sensing.[24–26] For humidity sensing, the introduction of an ion dopant in a composite material is effective to improve the response. However, chemiresistive humidity sensors in which ion species are periodically arranged *via* reversible coordination bonds to enhance their sensing performance are still rare, as are in-depth studies of their humidity sensing mechanism.

So far, electronically conductive coordination polymers with $(–M–S–)_n$ units have been developed as an effective strategy to design facile charge transport pathways in rigid CPs. Because the electronegativity of the chalcogen atoms and the transition metals are very well matched, facile charge transport pathways and good electrical conductivity can be achieved.[27–29] Therefore, the *p*-nitrothiophenol (*p*-NO_2PhSH) ligand and the transition metal Ag were selected for the construction of a conductive CP. Herein, a new silver-based 3D conductive coordination polymer, Ag(SPh–NO_2)·$AgNO_3$ (SPh–NO_2 = deprotonated *p*-nitrothiophenol) with abundant coordinated ionic species (Ag^+ and NO_3^-) was designed and synthesized, and showed exceptionally high moisture responsiveness and high stability as a chemiresistive humidity sensor. In addition, the electronic conductivity measurements indicate that it is a typical semiconductor with an electronic conductivity of 2.7×10^{-6} S cm^{-1} at room temperature. The chemiresistive humidity sensing of Ag(SPh–NO_2)·$AgNO_3$ was studied over a wide relative humidity (RH) range (10–90% RH). The sensor exhibited an exceptionally high moisture responsiveness of 10^6 times at 90% RH and an excellent sensitivity to humidity in the range of 10–80% RH. Its excellent humidity sensing is closely related to its hydrophilic surface and abundant coordinated ionic species. Furthermore, the sensing mechanism was investigated using alternating current impedance spectroscopy and direct current instantaneous reverse polarity experiments. The results revealed that the exceptionally high response of the Ag(SPh–NO_2)·$AgNO_3$-based sensor at high RH can be attributed to the periodic arrangement of ion species *via* reversible coordination bonds in its structure. H_3O^+ and Ag^+ are easily formed on its hydrophilic surface, through which the free transport of ionic carriers dominates the conductivity change. DFT calculations further demonstrate that the reversibly coordinated $AgNO_3$ in the structure can be easily occupied by water molecules, which is thermodynamically spontaneous in the presence of humidity. Moreover, the functional $AgNO_3$ group and its reversible coordination bond enabled Ag(SPh–NO_2)·$AgNO_3$ to show exceptionally high moisture responsiveness, which demonstrates the key role of reversible coordination bonding in a CCP for chemiresistive humidity sensing for the first time.

Experimental section

Materials

All reagents used in this work were purchased commercially. *p*-Nitrothiophenol was purchased from Aladdin (China). Silver nitrate ($AgNO_3$) and absolute ethanol were purchased from Sino pharm Group Co., Ltd. (China). The device substrate with a size of 3.5 mm × 7 mm was purchased from Beijing Elite Tech Co. (China). On the substrate are five pairs of parallel Ag–Pd interdigital electrodes with a distance of 0.2 mm.

Synthesis of Ag(SPh–NO_2)·$AgNO_3$ single crystals (1)

Crystal **1** was synthesized using a solvothermal method. Typically, 7.9 mg (0.05 mmol) of *p*-NO_2PhSH and 68 mg (0.4 mmol) of $AgNO_3$ were mixed in a 10 mL glass vial with 8 mL of ethanol. After sonication for 5 minutes, the reaction was kept in an oven at 85 °C for 12 hours. The resulting rod-like yellow crystals were washed with absolute ethanol and deionized water 3–5 times and dried at room temperature. The average yield of the crystal (relative to the ligand) was 89%. One crystal was chosen for single crystal X-ray crystallography analysis. Elem. Anal. found for Ag(SPh–NO_2)·$AgNO_3$ (%): C, 16.32%; H, 0.72%; N, 6.36%; S, 7.37%. Calcd (%): C, 16.68%; H, 0.93%; N, 6.49%; S, 7.42%.

Single crystal structure determination

The crystal structure of **1** was determined by SXRD measurement performed on a Rigaku Oxford Diffraction Supernova X-ray source diffractometer using graphite-monochromated Mo-Kα radiation with a λ of 0.07103 Å. The intensity data set was collected using a multi-scan technique and corrected for Lp effects. The primitive structure was solved by direct methods and refined by least-squares refinement on F^2 using the SHELXTL-2016 program package.[30] All non-hydrogen atoms were refined anisotropically. All hydrogen atoms on carbon were geometrically generated. Crystallographic data has been deposited with the Cambridge Crystallographic Data Centre, CCDC number: 2052741. Detailed crystallographic data are presented in Table 1, and additional bond angles and distances are shown in Tables S1 and S2.†

Characterization

Powder X-ray diffraction (PXRD) was conducted using Rigaku MiniFlex 600 diffractometers (Japan) with a Cu Kα target. The 2θ diffraction angle range and step size were set to 5–65° and 0.02°, respectively. The morphologies of compound **1** crystals were observed using a scanning electron microscope (SEM, ZEISS-300). Fourier transform infrared spectroscopy (FT-IR) measurements were performed with a Bruker VERTEX 70 FTIR spectrometer (Germany) using KBr tablets over the wavenumber range from 4000 to 400 cm^{-1}. Thermogravimetric (TG) analysis was conducted using a NETZSCHSTA449F3 analyzer (Germany). The sample was heated from 20 °C to 1000 °C at a 20 °C min^{-1} heating rate,

Table 1 Crystal and structure refinement data for crystal **1**

Crystal data	$Ag(SPh–NO_2)·AgNO_3$
Empirical formula	$C_6H_4Ag_2N_2O_5S$
Formula weight	431.91
Temperature	293(2) K
Wavelength	0.71073 Å
Crystal system	Monoclinic
Space group	$P2_1/n$
Unit cell dimensions	a = 13.896(3) Å, α = 90° b = 4.859(11) Å, β = 111.44° c = 15.280(4) Å, γ = 90°
Volume	960.4(4) Å^3
Z	4
Calculated density	2.987 Mg m^{-3}
Absorption coefficient	4.300 mm^{-1}
F(000)	816
Theta range for data collection	4.001° to 29.114°
Limiting indices	$-19 \le h \le 19$; $-6 \le k \le 6$; $-20 \le l \le 20$
Reflections collected/unique	13 794/2573 [$R_{(int)}$ = 0.0606]
Completeness to theta = 25.242	99.7%
Data/restraints/parameters	2573/0/145
GOF on F^2	1.038
Final R indices [$I > 2$ sigma(I)]	R_1 = 0.0436, wR_2 = 0.0736
R indices (all data)	R_1 = 0.0660, wR_2 = 0.0796

$R_1 = \sum||F_o| - |F_c||/\sum|F_o|$, $wR_2 = [\sum(|F_o|^2 - |F_c|^2)/\sum|F_o|^2]^{1/2}$.

and the N_2 flow rate was set to 20 mL min^{-1}. The gas adsorption–desorption isotherm test was performed using a BSD-PS1 gas adsorption instrument. High-purity N_2 was used in the adsorption experiment, and the gas isotherm was measured at 77 K. Solid-state UV-vis diffuse reflectance spectra (DRS) were acquired using a Lambda 950 (PerkinElmer, USA), and $BaSO_4$ was used as a blank standard. *I–V* curves of single crystal **1** at various temperatures were measured using a Keithley 4200 (USA) semiconductor characterization system *via* a two-probe DC method (see ESI† for electronic conductivity measurement details).

Chemiresistive humidity sensing measurements (DC method)

Crystals of **1** were ground with petroleum ether to form a viscous dispersion in an agate mortar. The dispersion was then drop-cast onto Al_2O_3 substrates with Ag–Pd interdigital electrodes to form a thin film sensing layer with a uniform thickness. Before testing, the devices were degassed under vacuum at 85 °C for 12 h. The sensors were measured in a custom-built sensing system that we have previously reported.[31] The sensor devices were placed in an opaque sealed quartz chamber at room temperature and dry air was used as the carrier gas for moisture. The DC current changes of the device under different relative humidity values were monitored to perform humidity sensing experiments. The sensor device was measured using a DC circuit with an applied bias of 1 V using a Keithley 2602B (USA) source meter. Humid gas was introduced into the quartz tube with a flow rate of 100–600 mL min^{-1} *via* mass flow controllers. The flow and relative humidity could be controlled using the mass flow controllers (see ESI† and Fig. S1 for details of the humidity control method). All of the sensing measurements were performed at ambient conditions.

Theoretical calculations

The Dmol^3 package was utilized to compute the electronic structure of the material.[32,33] All calculations were performed with the PBE exchange–correlation functional (the 1996 functional of Perdew, Burke and Ernzerhof) on periodically repeated slabs.[34] The double-numeric quality basis set with polarization functions (DNP) was adopted.[35–37] The numerical basis sets can minimise the basis-set superposition error.[38] A Fermi smearing of 0.005 hartree was utilized. The tolerances of the energy, gradient and displacement convergence were 1×10^{-5} hartree, 2×10^{-3} hartree per Å, and 5×10^{-3} Å, respectively.

Results and discussion

Crystal structure descriptions

Single crystals of compound **1** were synthesized *via* a solvothermal method with $AgNO_3$ and *p*-nitrothiophenol as reactants in absolute ethanol at 85 °C. The SXRD studies reveal that the space group of the compound **1** crystal is monoclinic $P2_1/n$. The compound possesses a nonporous 3D structure, which is formed by the connection of inorganic layers with 2D layered structures (Fig. 1b) and an organic layer made of *p*-nitrothiophenol. As shown in Fig. 1a and c, there are two crystallographically independent Ag^I ions (Ag1 and Ag2) in the asymmetric structural unit, and they are located in slightly distorted tetrahedron (Ag1) and tetragonal pyramid (Ag2) coordination environments, respectively. The four-coordinated Ag^I ions (Ag1) are coordinated with three μ_4-bridging sulfur (S) atoms as well as one μ_2-bridging oxygen (O) atom. The five-coordinated Ag^I ions (Ag2) are coordinated with one O atom, three μ_2-bridging O atoms, and one μ_4-bridging S atom. The two independent Ag^I ions are connected by the S of the sulfhydryl group and the O of the nitrate, and these oxygen and sulfur atoms also connect the same Ag ions to form a non-porous 3D structure. The Ag–S bond distances ranged from 2.5057(10) to 2.8143(8) Å,[39,40] and the bond length of the Ag–O bond ranged from 2.5153(5) to 2.6538(6) Å. The bond angles of S–Ag–S, O–Ag–O, S–Ag–O are 100.287°(5)–141.848°(4), 50.019°(4)–149.039°(4), and 95.907°(6)–133.118°(8), respectively. In the 3D skeleton of compound **1**, the charge of the network is balanced by two Ag^I ions and NO_3^- and $-S^-$ groups.

PXRD was used to characterize the phase purity of compound **1**. As shown in Fig. 2a, all the peaks from the experimental PXRD pattern matched well with the simulated PXRD pattern, indicating that there were no impurity phases in the as-prepared sample. SEM imaging showed the rod-like morphology of the compound **1** crystals (Fig. S2†). FT-IR further confirmed its structure and purity. As shown in

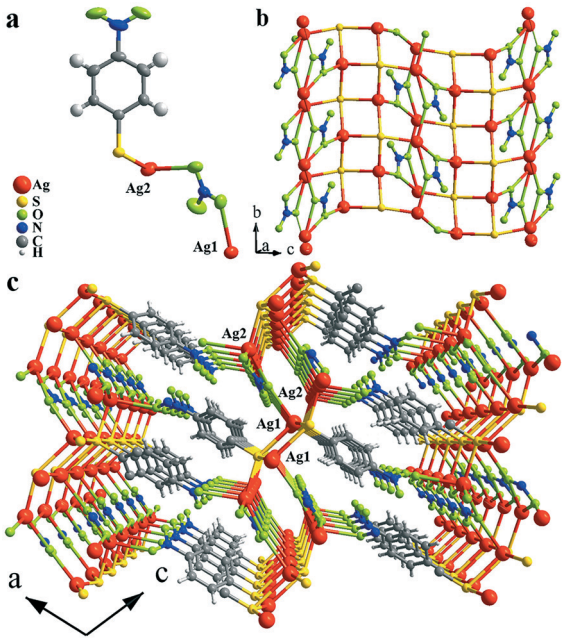

Fig. 1 The (a) structural unit and (b) 2D inorganic layer of compound **1**. (c) The 3D packing of compound **1** along the *ac* plane.

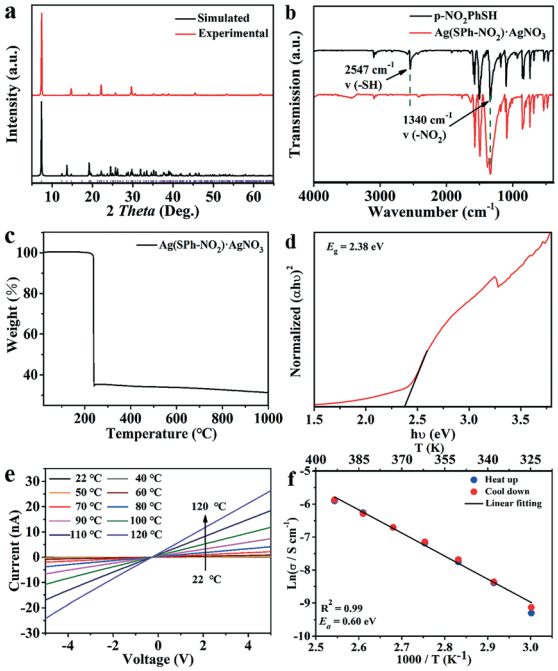

Fig. 2 Characterization of compound **1**. (a) Simulated and experimental PXRD patterns; (b) FT-IR patterns of compound **1** and the ligand *p*-NO_2PhSH; (c) the TG curve; (d) the optical band gap; (e) *I–V* curve testing in the range of 22–100 °C and (f) temperature-dependent electronic conductivity results for a single crystal of **1**.

Fig. 2b, compared with the spectra of the *p*-NO_2PhSH ligand, the –SH stretch vibration peak at 2547 cm^{-1} disappeared and the –NO_2 symmetrical absorption peak at 1340 cm^{-1} was split into two peaks in compound **1**, which indicates the coordination between ligands and Ag^I ions. The N_2 adsorption–desorption measurement at 77 K revealed that compound **1** is nonporous, which is consistent with the crystal structure (Fig. S3†). The specific surface area calculated from the N_2 adsorption measurement was 3.7615 $m^2\ g^{-1}$. The thermal stability of compound **1** was studied by TG analysis. Fig. 2c shows that compound **1** underwent weight loss from 235 to 800 °C in a N_2 atmosphere. This is indicated that compound **1** is stable below 235 °C without mass loss and contains no solvent molecules. The rapid weight loss of compound **1** after the temperature reached 235 °C could be ascribed to the decomposition of the non-metal components and the collapse of the whole framework.

Semiconducting properties

The DRS of the compound **1** shows an absorption band in the range of 200–521 nm (Fig. S4†) with an optical band gap (E_g) of 2.38 eV (Fig. 2d). The electronic conduction (*I–V* curves) was measured using the two-probe method with single crystal **1** (see ESI† for measurement details). Fig. 2e and f display the temperature-dependent conductive properties of single crystal **1** with a calculated activation energy (E_a) of 0.60 eV (see ESI† for related formula). The electronic conductivity of single crystal **1** at a room temperature of 295 K is approximately 2.7×10^{-6} S cm^{-1} (Fig. S5†). The possible conduction path for electrons in the structure of crystal **1** is shown in the ESI† and Fig. S6.

Humidity sensing performance analysis (DC method)

The humidity sensing performance of compound **1** was first investigated at room temperature. Fig. 3a shows the typical real-time dynamic response–recovery curve of the compound **1**-based humidity sensor over a broad RH range of 10% to 90% RH. Additionally, it should be mentioned that the sensor shows good response–recovery characteristics in this humidity range with a good signal-to-noise ratio. When the inflow of humid air begins, the current of the sensor increases immediately, and then gradually tends to become stable. Once the humid air is switched to dry air, the current immediately returns to the baseline current of 10^{-12} A. The response value of the sensor toward humidity is defined as the ratio of the sensor resistance in dry gas to that in humid gas:

$$\text{Response} = R_{dry}/R_{humidity} - 1 = I_{humidity}/I_{dry} - 1 \quad (1)$$

Fig. 3b shows the response–RH% plot of the sensor based on compound **1**, indicating that the response value can reach up to 10^6 at 90% RH. To the best of our knowledge, this responsiveness is the highest response among the reported humidity sensors (Table S3†). Fig. 3c shows the response–recovery plot in 80% RH over five continuous cycles, which indicates the good repeatability of this sensor with a coefficient of variation (CV) value of 7.2%. The response and recovery time (the response time of the sensor refers to the time required for the response to reach 90% of its saturation value, and the recovery time refers to the time required for

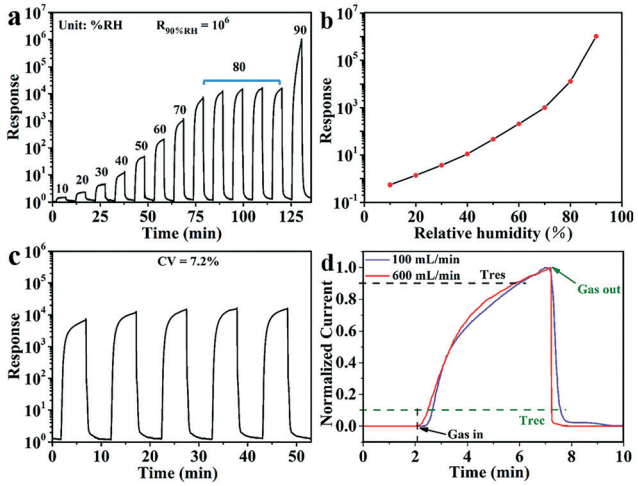

Fig. 3 Chemiresistive humidity sensing measurements at room temperature using the DC method. (a) The response–recovery curve of compound **1** for 10–90% RH. (b) A plot of the RH response of compound **1**. (c) The response–recovery curve for five consecutive cycles under 80% RH. (d) The response and recovery times at 80% RH at 100 and 600 mL min^{-1}.

the response to recover to 10% of its saturation value) of the compound-**1**-based sensor to 80% RH at a gas flow of 600 mL min^{-1} were calculated to be 3.30 min and 5.00 s (Fig. 3d). The extremely short recovery time is faster than that of most CP-based humidity sensors, and is even comparable to that of metal oxide or carbon-based sensors (Table S3†). The fast recovery speed of compound **1** may be due to its nonporous nature, and its surface H_2O molecules may be removed easily under a dry air flow. In addition, the effects of flow rate on the response and recovery speed were also studied. When the gas flow was decreased to 100 mL min^{-1}, the response and recovery time increased to 3.99 min and 29.40 s, respectively (Fig. 3d). This phenomenon can be attributed to the different concentration gradient induced by the gas flow. Generally, the higher the concentration gradient imposed between the device and the target atmosphere, the faster the response and recovery time obtained.

In order to explore the stability under high humidity, the PXRD of compound **1** was studied before and after exposure to the 100% RH condition for 24 hours. As shown in Fig. 4a, b and S7,† the positions of its PXRD peaks and morphology did not change, indicating the robustness of compound **1** under high-humidity conditions. Furthermore, a time-dependent contact angle test of compound **1** was conducted to characterize its hydrophilic properties. As shown in Fig. 4c, the initial contact angle is 61°, and the contact angle then gradually decreases until the water drop is completely adsorbed, which demonstrates the hydrophilic characteristics of compound **1**.

Humidity sensing mechanism

For sensing materials, the study of surface-absorbed water molecules is of great significance to illuminate the sensing mechanism.[32,41–43] The humidity related change in conduction is known to be strongly linked to the chemical and subsequent physical absorption of water molecules on the surface. $Ag(SPh–NO_2)·AgNO_3$ possesses a 2D inorganic layered structure with closely packed organic linkers that form a 3D nonporous robust structure. Its exceptionally high moisture responsiveness under high relative humidity prompted us to do further sensing mechanism research. In addition, due to its hydrophilic nature, the external surfaces of this CP crystal are available to absorb water molecules. Hence, its humidity sensing mechanism was mainly derived from its outer surfaces.

To investigate the humidity sensing mechanism of $Ag(SPh–NO_2)·AgNO_3$, AC impedance spectra were measured from 0.1 Hz to 10^5 Hz at various humidity levels (Fig. 5) (see ESI† for measurement details). As shown in Fig. 5a with 40% RH, the Nyquist plot appeared as part of a semicircle, which can be fitted by an equivalent circuit consisting of a parallel resistor (R) and capacitor (C). At this stage, only a few water molecules are absorbed on the crystal surface and the main conductive ions were a few protons (H^+) transported *via* hopping from site to site, thus leading to low proton conduction. At intermediate humidity levels (60%, 75% RH), more water molecules were absorbed on the surface due to the hydrophilic surface of this compound. The Nyquist plots exhibited smaller semicircles at high frequency (HF) and a short tail on the semicircle at low frequency (LF) (Fig. 5b and c). The short tail represented the Warburg Impedance, indicating the diffusion of ions and charge carriers at the interface between the sensing materials and electrodes. During this process, plentiful H_3O^+ was formed ($H^+ + H_2O \rightarrow H_3O^+$) because more water molecules were absorbed.[44] According to the Grotthuss mechanism, the transfer of H_3O^+ becomes easier with a dramatic decrease of impedance. With the further increase of the RH (85%, 90% and 95% RH), the Nyquist plots showed two semicircles at HF and a short tail at LF (Fig. 5d–f). During this process, a multilayer water film was formed, resulting in the ionization of Ag^+ and the growth of a surface ionic layer (SIL) at the crystal particle/water film. The ionic conduction came from

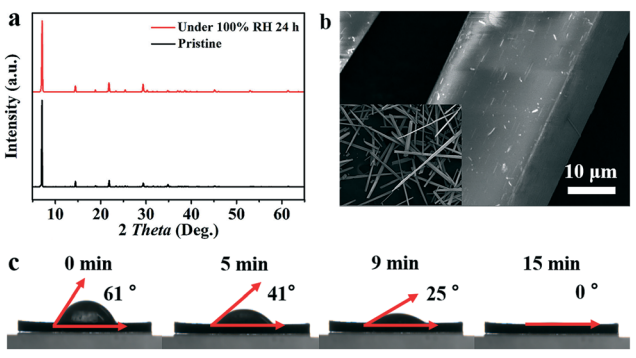

Fig. 4 (a) PXRD and (b) SEM patterns for compound **1** at 100% RH for 24 hours. (c) Time-dependent contact angle testing of a compound **1** pellet.

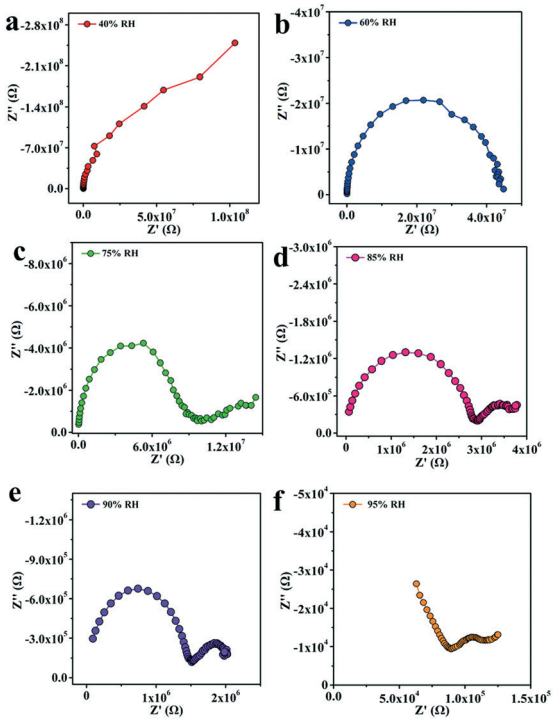

Fig. 5 Nyquist plots of the compound-1-based sensor obtained from 0.1 Hz to 10^5 Hz at (a) 40%, (b) 60%, (c) 75%, (d) 85%, (e) 90%, and (f) 95% RH.

Ag^+ and resulted in a sharp decrease in the impedance of the sensor. The low-frequency semicircle (right semicircle) observed is assigned to the combination of charge transfer resistance of $Ag(SPh–NO_2)·AgNO_3$ and surface SIL layer

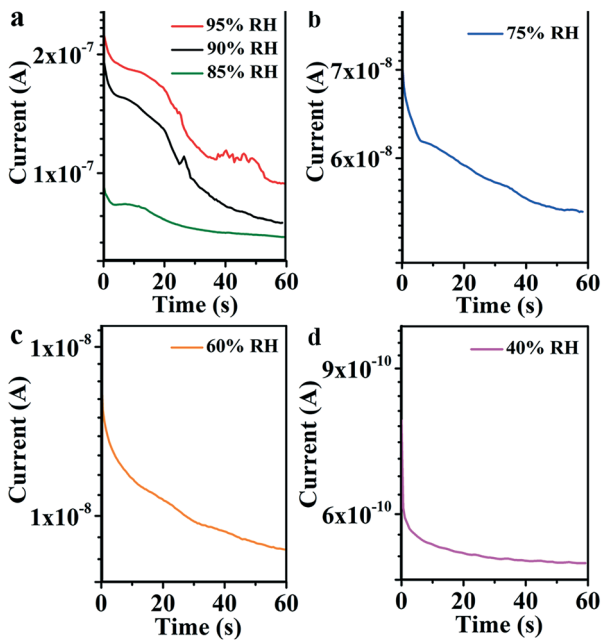

Fig. 6 Current–time curves of the compound-1-based sensor at (a) 95%, 90%, 85%, (b) 75%, (c) 60%, and (d) 40% RH obtained using DC instantaneous reverse polarity experiments.

Table 2 Gibbs free energy (ΔG) values for the reaction $Ag(SPh–NO_2)·AgNO_3 + nH_2O \rightarrow AgNO_3 + Ag(SPh–NO_2)·nH_2O$ with different n values

	$n(H_2O)$	1	2	3	4	5	6
(001)	ΔG/eV	0.88	−0.08	−0.52	−1.14	−1.58	−2.14
(010)	ΔG/eV	1.31	0.87	0.24	−0.30	−1.10	−1.72

resistance. It is reasonable to assign the high-frequency semicircle (left semicircle) to the impedance of the electrified interface between the crystal surface structure and the ionic layer involving the reversible coordination process of the Ag^+/NO_3^- ions coupled with electron transfer and migration in the crystal.

In order to verify the results of the AC impedance spectra measurements, DC instantaneous reverse polarity experiments were performed (see ESI† for measurement details). The corresponding DC circuit is shown in Fig. S9† with a bias voltage of 5 V. The humidity sensor connected to DC will form the space charge acting as the conductive ions. When the polarity of DC is changed, the dominant conductive ions are transferred to the opposite pole, leading to a current peak when they reach the other electrode. The number of current peaks corresponds to the kinds of conductive species under various RH conditions.[45] The current–time curves at various RH conditions are shown in Fig. 6.

The total current of each curve consists of two parts: the ion conduction current in the initial stage and the electron conduction current in the steady stage.[46] Under low humidity (40% RH), there was little H^+, and it was not continuous, with no current peak being observed. At moderate humidity (60% and 75% RH), as more water molecules were adsorbed on the crystal surface, a small peak corresponding to the transfer of H_3O^+ appeared. As the humidity was further increased (85%, 90% and 95% RH), a continuous water layer was formed. Two current peaks corresponding to the transfer of H_3O^+ and Ag^+ were observed.[47] The results show that for the chemiresistive humidity sensor based on $Ag(SPh–NO_2)·AgNO_3$, the free transport of ionic carriers dominates the change in conductivity.

DFT calculations

The (001) and (010) planes, cleaved in 1 × 2 unit cells of $Ag(SPh–NO_2)·AgNO_3$, were used in this work. The periodic boundary condition was set at 15 Å. All structures were fully relaxed to the ground state. The Gibbs free energy (ΔG) for the reaction $Ag(SPh–NO_2)·AgNO_3 + nH_2O \rightarrow AgNO_3 + Ag(SPh–NO_2)·nH_2O$ was calculated. When two and four water molecules occupy the $AgNO_3$ site on (001) and (010) crystal planes, the calculated Gibbs free energy values were −0.08 eV and −0.03 eV, respectively, which means that the reaction is thermodynamically spontaneous. The more water present, the more easily this reaction occurs. When n = 1, 2, 3, 4, 5 and 6, for the (001) plane, ΔG/eV = 0.88, −0.08, −0.52, −1.14, −1.58 and −2.14; for the (010) plane, ΔG/eV = 1.31, 0.87, 0.24, −0.30, −1.10 and −1.72, as shown in Table 2 and Fig. S10.†

Conclusions

In conclusion, a new 3D conductive coordination polymer, $Ag(SPh–NO_2)·AgNO_3$, has been successfully synthesized and characterized. This compound exhibits typical semiconducting behavior, with electronic conductivity of 2.7×10^{-6} S cm^{-1} at room temperature, which is superior to most major 3D CCPs. Furthermore, due to its nonporous structure, semiconducting characteristics, and abundant ionic species, it is an ideal candidate to act as a humidity sensor. The humidity sensing of $Ag(SPh–NO_2)·AgNO_3$ was studied over a wide range of relative humidity values (10–90%) at room temperature. The sensor exhibited exceptionally high moisture responsiveness, with a 10^6-fold increase in the response at 90% RH and excellent sensitivity to humidity in the range of 10–80% RH. The sensing mechanism study showed that the exceptionally high response of the $Ag(SPh–NO_2)·AgNO_3$-based sensor at high RH is attributable to the periodic arrangement of its ion species *via* reversible coordination bonds in the structure. H_3O^+ and Ag^+ are easily formed on its hydrophilic surface, through which the free transport of ionic carriers dominates the change in conductivity. DFT calculations further demonstrate that the presence of functional $AgNO_3$ groups and its reversible coordination bonding enabled $Ag(SPh–NO_2)·AgNO_3$ to show exceptionally high moisture responsiveness, which is the first time that the key role of the reversible coordination bonds in CCPs for chemiresistive humidity sensing has been demonstrated. Finally, it is expected that this study will provide *a* direction for the development of high-performance humidity sensors based on semiconducting coordination polymers.

Conflicts of interest

The authors declare no competing financial interests.

Acknowledgements

This work was supported by the National Natural Science Foundation of China (21805276, 21822109, 2020000052, 21905280, 21975254, 21950410532, 24074283), Key Research Program of Frontier Science, CAS (QYZDB-SSW-SLH023), International Partnership Program of CAS (121835KYSB201800), the Natural Science Foundation of Fujian Province (2017J05094), the Youth Innovation Promotion Association CAS (2018342), China Post-doctoral Science Foundation (2019M662254), and Special Research Assistant Program of the Chinese Academy of Sciences.

References

1 D. Helbing, *Nature*, 2013, **497**, 51–59.
2 J. F. Fennell Jr., S. F. Liu, J. M. Azzarelli, J. G. Weis, S. Rochat, K. A. Mirica, J. B. Ravnsbaek and T. M. Swager, *Angew. Chem., Int. Ed.*, 2016, **55**, 1266–1281.
3 A. Kaushik, R. Kumar, S. K. Arya, M. Nair, B. D. Malhotra and S. Bhansali, *Chem. Soc. Rev.*, 2015, **115**, 4571–4606.
4 W.-T. Koo, J.-S. Jang and I.-D. Kim, *Chem*, 2019, **5**, 1938–1963.
5 J. Wu, J. Chen, C. Wang, Y. Zhou, K. Ba, H. Xu, W. Bao, X. Xu, A. Carlsson, S. Lazar, A. Meingast, Z. Z. Sun and H. X. Deng, *Adv. Sci.*, 2020, **7**, 1903003.
6 S. W. Chiu and K. T. Tang, *Sensors*, 2013, **13**, 14214–14247.
7 R. Kostiainen, *Atmos. Environ.*, 1995, **29**, 693–702.
8 Y. Liu, R. Bao, J. Tao, J. Li, M. Dong and C. Pan, *Sci. Bull.*, 2020, **65**, 70–88.
9 Kenry, J. C. Yeo and C. T. Lim, *Microsyst. Nanoeng.*, 2016, **2**, 16043.
10 P. Wang and Q. Liu, *Biomedical Sensors and Measurement*, Springer, Berlin, 2011, pp. 51–115.
11 G. F. Fine, L. M. Cavanagh, A. Afonja and R. Binions, *Sensors*, 2010, **10**, 5469–5502.
12 Z. Zhao, J. Tian, Y. Sang, A. Cabot and H. Liu, *Adv. Mater.*, 2015, **27**, 2557–2582.
13 K. Kalantar-zadeh, J. Z. Ou, T. Daeneke, A. Mitchell, T. Sasaki and M. S. Fuhrer, *Appl. Mater. Today*, 2016, **5**, 73–89.
14 C. N. R. Rao, *Annu. Rev. Phys. Chem.*, 1989, **40**, 291–326.
15 F. M. Wisser, J. Grothe and S. Kaskel, *Sens. Actuators, B*, 2016, **223**, 166–171.
16 W. Yuan, A. Liu, L. Huang, C. Li and G. Shi, *Adv. Mater.*, 2013, **25**, 766–771.
17 H. Peng, F. Li, Z. Hua, K. Yang, F. Yin and W. Yuan, *Sens. Actuators, B*, 2018, **275**, 78–85.
18 E. Lee, Y. S. Yoon and D. J. Kim, *ACS Sens.*, 2018, **3**, 2045–2060.
19 D. Sarkar, X. Xie, J. Kang, H. Zhang, W. Liu, J. Navarrete, M. Moskovits and K. Banerjee, *Nano Lett.*, 2015, **15**, 2852–2862.
20 Z. Yang, A. Liu, C. Wang, F. Liu, J. He, S. Li, J. Wang, R. You, X. Yan, P. Sun, Y. Duan and G. Lu, *ACS Sens.*, 2019, **4**, 1261–1269.
21 A. M. Spokoyny, D. Kim, A. Sumrein and C. A. Mirkin, *Chem. Soc. Rev.*, 2009, **38**, 1218–1227.
22 H.-N. Wang, X. Meng, L.-Z. Dong, Y. Chen, S.-L. Li and Y.-Q. Lan, *J. Mater. Chem. A*, 2019, **7**, 24059–24091.
23 D. Tanaka, A. Henke, K. Albrecht, M. Moeller, K. Nakagawa, S. Kitagawa and J. Groll, *Nat. Chem.*, 2010, **2**, 410–416.
24 X.-J. Lv, M.-S. Yao, G.-E. Wang, Y.-Z. Li and G. Xu, *Sci. China: Chem.*, 2017, **60**, 1197–1204.
25 J. H. Huang, Y. He, M.-S. Yao, J. He, G. Xu, M. Zeller and Z. Xu, *J. Mater. Chem. A*, 2017, **5**, 16139–16143.
26 T. Leelasree, V. Selamneni, T. Akshaya, P. Sahatiya and H. Aggarwal, *J. Mater. Chem. B*, 2020, **8**, 10182–10189.
27 Y. Z. Li, X. M. Jiang, Z. H. Fu, Q. Q. Huang, G. E. Wang, W. H. Deng, C. Wang, Z. Z. Li, W. J. Yin, B. L. Chen and G. Xu, *Nat. Commun.*, 2020, **11**, 261.
28 L. Sun, C. H. Hendon, M. A. Minier, A. Walsh and M. Dincă, *J. Am. Chem. Soc.*, 2015, **137**, 6164–6167.
29 A. Pathak, J. W. Shen, M. Usman, L. F. Wei, S. Mendiratta, Y. S. Chang, B. Sainbileg, C. M. Ngue, R. S. Chen, M. Hayashi, T. T. Luo, F. R. Chen, K. H. Chen, T. W. Tseng, L. C. Chen and K. L. Lu, *Nat. Commun.*, 2019, **10**, 1721.
30 Siemens, *SAINT., SHELXTL.*, Siemens Analytical X–ray Instruments Inc, Madison, Wisconsin, USA, 1994.

31 M. S. Yao, W. X. Tang, G. E. Wang, B. Nath and G. Xu, *Adv. Mater.*, 2016, **28**, 5229–5234.
32 H. Bi, K. Yin, X. Xie, J. Ji, S. Wan, L. Sun, M. Terrones and M. S. Dresselhaus, *Sci. Rep.*, 2013, **3**, 2714.
33 B. Delley, *J. Chem. Phys.*, 2000, **113**, 7756–7764.
34 P. P. John, B. Kieron and M. Ernzerhof, *Phys. Rev. Lett.*, 1996, **77**, 3865–3868.
35 B. Delley, *J. Chem. Phys.*, 1990, **92**, 508–517.
36 L. Versluis and T. Ziegler, *J. Chem. Phys.*, 1988, **88**, 322–328.
37 U. V. Barth and L. Hedin, *J. Phys. C: Solid State Phys.*, 1972, **5**, 1629–1642.
38 N. Matsuzawa, J. Seto and D. A. Dixon, *J. Phys. Chem. A*, 1997, **101**, 9391–9398.
39 R. M. Silva, M. D. Smith and J. R. Gardinier, *Inorg. Chem.*, 2006, **45**, 2132–2142.
40 S. S. Babadi, A. Beheshti, M. B. Pour, P. Mayer, H. Motamedi, D. Trzybiński and K. Wozniak, *Cryst. Growth Des.*, 2019, **19**, 4934–4948.
41 Y. Y. Yin, L. X. Zhang, H. Xu, Y. C. Jian, M. J. Zhang and L. J. Bie, *Inorg. Chem. Commun.*, 2021, **125**, 108440.
42 L. Liu, C. Zhang, L. X. Zhang, Q. Li, Y. Y. Yin, H. Y. Wang, R. H. Sun, J. Y. Li, X. Y. Hou, H. Dong and L. J. Bie, *Inorg. Chem. Commun.*, 2020, **111**, 107636.
43 P. Zhang, L. X. Zhang, H. Xu, Y. Xing, J. J. Chen and L. J. Bie, *Rare Met.*, 2021, **40**, 1614–1621.
44 F. M. Ernsberger, *J. Am. Ceram. Soc.*, 1983, **66**, 747–750.
45 J. Wang and G. Song, *Thin Solid Films*, 2007, **515**, 8776–8779.
46 Y. C. Yeh and T. Y. Tseng, *J. Mater. Sci.*, 1989, **24**, 2739–2745.
47 K. Jiang, H. Zhao, T. Fei, H. Dou and Z. Tong, *Sens. Actuators, B*, 2016, **222**, 440–446.

